PROCEEDINGS OF THE ROYAL SOCIETY A

rspa.royalsocietypublishing.org

Research

Article submitted to journal

Subject Areas:
xxxxx, xxxxx, xxxx

Keywords:
xxxx, xxxx, xxxx

Author for correspondence:
T. Roose
e-mail: t.roose@soton.ac.uk

Royal Society Publishing
Informing the science of the future

Determination of macro-scale soil properties from pore scale structures - Model derivation

K.R. Daly[1] and T. Roose[1]

[1]Bioengineering Sciences Research Group, Faculty of Engineering and the Environment, University of Southampton, Southampton SO17 1BJ, England, UK

In this paper we use homogenisation to derive a set of macro-scale poro-elastic equations for soils composed of rigid solid particles, air filled pore-space and a poro-elastic mixed phase. We consider the derivation in the limit of large deformation and show that by solving representative problems on the micro-scale we can parametrise the macro-scale equations. To validate the homogenisation procedure we compare the predictions of the homogenised equations to those of the full equations for a range of different geometries and material properties. We show that the results differ by $\lesssim 2\%$ for all cases considered. The success of the homogenisation scheme means that it can be used to determine the macro-scale poro-elastic properties of soils from the underlying structure. Hence, it will prove a valuable tool in both characterisation and optimisation.

1. Introduction

The properties of complex composite poro-elastic materials, for example soil, are often described using the theory of Biot [1–3]. This theory describes an elastic solid matrix saturated with a fluid by formulating the stress in terms of solid displacement and fluid pressure [4]. The necessary coefficients in the stress tensors can then be measured based on a series of mechanical tests [3]. The equations derived by Biot are widely used in poro-elasticity [4,5].

One area of particular interest is the field of soil mechanics. Soils are inherently multiscale in structure and the macroscopic poro-elastic properties are dependent on the precise details of the micro structure [6]. On the micro-scale techniques such as X-ray Computed Tomography are often used to aid understanding of soil properties [7,8]. Linking this micro-scale modelling to the macro-scale is an important challenge [9].

© The Author(s) Published by the Royal Society. All rights reserved.

It has been shown that the theory of Biot can be derived based on the underlying pore structure using homogenisation theory. This has been achieved for the case of small deformations [10], and has been extended to include large deformations through careful consideration of the deformed geometry [11]. The result is a non-linear version of the Biot poro-elastic equations. It has been shown that neglecting the nonlinear terms can seriously under estimate the pore water pressure in soft layers [12]. In addition, soils are rarely fully saturated and can have different properties depending on the moisture content [13], which can also vary locally due to the influence of plants [14]. A number of different Biot type models have been proposed to capture the properties of partially saturated porous media, see [15] and references therein. However, these are all continuum models and are not tied to the underlying porous structures.

In this paper we derive a method that allows the macroscopic mechanical behaviour of soil to be calculated from the underlying structure. Our aim is to derive a theory which links the micro-scale properties of the soil to the macro-scale. Hence, our starting point is a description of the soil which captures the movement or air and water on the micro-scale. We derive the macro-scale equations, assuming large deformation, using homogenisation theory. Homogenisation theory is a mathematical technique which allows macro-scale equations to be derived based on a set of representative equations, known as cell problems, which are solved on an underlying periodic micro-structure [16–18]. Homogenisation has been widely used in the field of porous media [16]. Typically it is used to describe saturated fluid flow [19,20], two phase flow [21], diffusion [22–24] and poro-elasticity [25]. In addition hierarchical homogenisation, in which multiple levels of homogenisation are applied, has been used to describe fluid flow [26] and poro-elasticity [27].

Here, our starting point is to consider the observable phases in a typical soil. Figure 1 shows an X-ray Computed Tomography image of a sandy loam soil, the most common soil in the UK. Typically poro-elasticity studies focus on two different interacting phases such as elastic solids and fluids [10,11], poroelastic materials and fluids [27] or viscoelastic materials and fluids [25]. However, in figure 1 we observe three different phases, rigid solid particles, air filled pore-space and a mixed phase composed of sub resolution particles and fluid. For clarity these phases have been highlighted as different colours in the right hand image. Whilst some papers consider the effective properties of three phase poro-elastic materials in the context of small deformations [28, 29], these are based on composite sphere assemblies that do not account for the geometrical details observed in Figure 1.

We consider the mixed phase as a poro-elastic mixture composed of elastic colloids and pore water [1,30]. We assume that the density and viscosity of the fluids are known, and the mixed phase has a known shear modulus, Poisson ratio and permeability. The solid particles move through rigid body translations and the air filled pore-space acts as a viscous fluid. Through application of homogenisation [17] we derive a set of macroscopic equations for the case of large structural deformation [11]. The homogenised equations are parameterised by a set of effective parameters. These parameters are determined from the underlying geometry through a series of four cell problems, which capture the Darcy flow of air, the Darcy flow of water , the effective stiffness, and the pressure induced stress in the mixed phase. From these, we derive parameters which describe the mobility of air and water, the soil stiffness, a set of pressure induced stress coefficients, and a series of parameters which determine the change in air and water volume due to pressure variations and strain. We show that the movement of the boundaries between the different phases produces a non-linear counterpart to these terms, in addition to the linear terms. Finally, we validate the homogenisation procedure by comparing the predictions of the original equations to the predictions of the homogenised version.

2. Theory

We consider the soil domain Ω to be composed of three domains: solid mineral phases, air and a mixed phase, see Figure 1. The mixed phase is composed of water and smaller mineral phases. We do not consider the fluid dynamics inside the mixed phase individually, rather we consider a

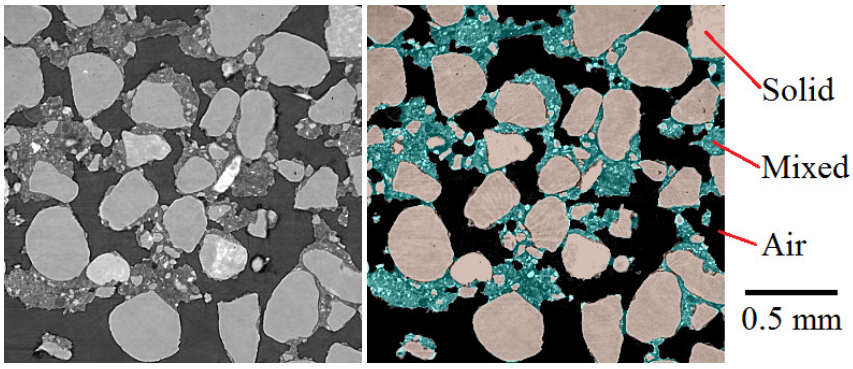

Figure 1. Domains used in poro-elastic theory. The left hand image shows a single X-ray Computed Tomography slice. The image on the right shows a segmented overlay of the solid, mixed and air phases.

set of averaged equations which describe this region. We denote the solid, mixed and air phases Ω_s, Ω_m and Ω_a respectively such that $\Omega = \Omega_m \cup \Omega_s \cup \Omega_a$. The solid phase is composed of a set of smaller particles $\Omega_s = \cup \Omega_{s,j} \forall j$. The interfaces between these regions are defined as Γ_{am}, Γ_{as} and Γ_{ms} for the air-mixed, air-solid and mixed-solid interfaces respectively. Again the solid boundaries are given as the union of all solid boundaries $\Gamma_{ms} = \cup \Gamma_{ms,j} \forall j$ and $\Gamma_{as} = \cup \Gamma_{as,j}$. We also define $\hat{\boldsymbol{n}}^{am}$ as the unit normal vector on the air–mixed phase interface pointing into the mixed phase domain, $\hat{\boldsymbol{n}}^{as}$ as the unit normal vector on the air–solid interface pointing into the solid domain, and $\hat{\boldsymbol{n}}^{ms}$ as the unit normal vector on the mixed phase–solid interface pointing into the solid domain.

We write the total displacement of the mixed phase as $\tilde{\boldsymbol{u}}^{tot} = \phi \tilde{\boldsymbol{u}}^w + (1-\phi)\tilde{\boldsymbol{u}}^m$, where ϕ is the porosity of the mixed phase, $\tilde{\boldsymbol{u}}^m$ is the displacement of the solid fraction of the mixed phase and $\tilde{\boldsymbol{u}}^w$ is the displacement of the liquid fraction of the mixed phase. The mixed phase is described by conservation of momentum

$$\tilde{\boldsymbol{\nabla}} \cdot \tilde{\sigma}^m - \tilde{\boldsymbol{\nabla}} \tilde{p}^w = \left[\phi \rho^w + (1-\phi)\rho^m\right] g \hat{\boldsymbol{e}}_3, \qquad \tilde{\boldsymbol{x}} \in \Omega_m, \tag{2.1a}$$

where the stress tensor is written as

$$\tilde{\sigma}^m = G\tilde{e}(\tilde{\boldsymbol{u}}^m) + \frac{\nu G}{1-2\nu} \tilde{\boldsymbol{\nabla}} \cdot \tilde{\boldsymbol{u}}^m I, \qquad \tilde{\boldsymbol{x}} \in \Omega_m, \tag{2.1b}$$

ρ^w is the water density, ρ^m is the density of the solid part of the mixed phase, I is the identity matrix, g is the acceleration due to gravity, $\hat{\boldsymbol{e}}_3$ is a unit vector in the vertical direction, $\tilde{e}(\tilde{\boldsymbol{u}}^m) = \left(\tilde{\boldsymbol{\nabla}} \tilde{\boldsymbol{u}}^m\right) + \left(\tilde{\boldsymbol{\nabla}} \tilde{\boldsymbol{u}}^m\right)^T$ is the strain, ν is Poisson's ratio, G is the shear modulus of the mixed phase, $\tilde{p}^w$ is the water pressure and a tilde denotes a dimensional variable. Conservation of mass for each phase yields

$$\frac{\partial \phi}{\partial \tilde{t}} = -\tilde{\boldsymbol{\nabla}} \cdot \phi \tilde{\boldsymbol{v}}^w, \qquad \tilde{\boldsymbol{x}} \in \Omega_m, \tag{2.1c}$$

$$-\frac{\partial \phi}{\partial \tilde{t}} = -\tilde{\boldsymbol{\nabla}} \cdot (1-\phi)\tilde{\boldsymbol{v}}^m, \qquad \tilde{\boldsymbol{x}} \in \Omega_m, \tag{2.1d}$$

and Darcy's law for the relative phase velocity can be written as

$$\phi\left(\tilde{\boldsymbol{v}}^w - \tilde{\boldsymbol{v}}^m\right) = -\frac{k}{\mu^w}\left(\tilde{\boldsymbol{\nabla}} \tilde{p}^w + \rho^w g \hat{\boldsymbol{e}}_3\right), \qquad \tilde{\boldsymbol{x}} \in \Omega_m. \tag{2.1e}$$

where μ^w is the water viscosity, k is the permeability of the mixed phase and the velocities are defined as

$$\tilde{\boldsymbol{v}}^m = \frac{\partial \tilde{\boldsymbol{u}}^m}{\partial \tilde{t}} + \tilde{\boldsymbol{v}}^m \cdot \tilde{\boldsymbol{\nabla}} \tilde{\boldsymbol{u}}^m, \qquad \tilde{\boldsymbol{x}} \in \Omega_m \tag{2.1f}$$

and

$$\tilde{\boldsymbol{v}}^w = \frac{\partial \tilde{\boldsymbol{u}}^w}{\partial \tilde{t}} + \tilde{\boldsymbol{v}}^w \cdot \tilde{\boldsymbol{\nabla}} \tilde{\boldsymbol{u}}^w, \qquad \tilde{\boldsymbol{x}} \in \Omega_m. \tag{2.1g}$$

Adding equations (2.1*c*) to (2.1*d*), assuming k/μ^w constant and taking the divergence of (2.1*e*) we obtain

$$\frac{k}{\mu^w} \tilde{\boldsymbol{\nabla}} \cdot \left(\tilde{\boldsymbol{\nabla}} \tilde{p}^w + \rho^w g \hat{\boldsymbol{e}}_3 \right) = \tilde{\boldsymbol{\nabla}} \cdot \boldsymbol{v}^m, \qquad \tilde{\boldsymbol{x}} \in \Omega_m. \tag{2.2}$$

In the air phase we write down the incompressible Stokes' equations for fluid velocity and pressure

$$\tilde{\boldsymbol{\nabla}} \cdot \tilde{\sigma}^a - \tilde{\boldsymbol{\nabla}} \tilde{p}^a = \rho^a g \hat{\boldsymbol{e}}_3, \qquad \tilde{\boldsymbol{x}} \in \Omega_a, \tag{2.3a}$$

$$\tilde{\sigma}^a = \mu^a \tilde{e}(\tilde{\boldsymbol{v}}^a), \qquad \tilde{\boldsymbol{x}} \in \Omega_a, \tag{2.3b}$$

$$\tilde{\boldsymbol{\nabla}} \cdot \tilde{\boldsymbol{v}}^a = 0, \qquad \tilde{\boldsymbol{x}} \in \Omega_a, \tag{2.3c}$$

where $\tilde{\boldsymbol{v}}^a$ and $\tilde{p}^a$ are the air velocity and pressure respectively, μ^a is the air viscosity and ρ^a is the air density. Next we consider the solid fraction, this component is free to translate as a rigid body. Hence, it must satisfy the equations

$$\tilde{\boldsymbol{u}}^{s,j} = \text{const}_j, \qquad \tilde{\boldsymbol{x}} \in \Omega_s, \tag{2.4a}$$

$$\int_{\Gamma_{ms,j}} \hat{\boldsymbol{n}}^{ms} \cdot \tilde{\sigma}^{s,j} \, dx + \int_{\Gamma_{as,j}} \hat{\boldsymbol{n}}^{as} \cdot \tilde{\sigma}^{s,j} \, dx = -\rho^s g \int_{\Omega_{s,j}} 1 \, dx \hat{\boldsymbol{e}}_3, \qquad \tilde{\boldsymbol{x}} \in \Omega_s, \tag{2.4b}$$

where ρ^s is the density of the solid assumed constant across all grains, $\tilde{\boldsymbol{u}}^{s,j}$ and $\tilde{\sigma}^{s,j}$ are the displacement and stress of the j-th solid. We note that we do not consider shear forces between two different solid grains. It is assumed throughout that there is always a thin layer of the mixed phase between any two solid particles. We express the condition $\tilde{\boldsymbol{u}}^s = \text{const}$ as a condition on the tangential variation on the surface

$$\sum_{k=1}^{2} \left(\hat{\boldsymbol{\tau}}_k \cdot \tilde{e}(\tilde{\boldsymbol{u}}^{s,j}) \cdot \hat{\boldsymbol{e}}_p \right)^2 = 0, \qquad \tilde{\boldsymbol{x}} \in \Gamma_{s,j}, \tag{2.5}$$

for $p = \{1, 2, 3\}$. Here $\hat{\boldsymbol{\tau}}_k$ for $k = \{1, 2\}$ are the unit tangent vectors on the surface solid surface.

(a) Boundary conditions

In order to complete the description of the coupled mixed phase–solid–fluid system we need a set of boundary conditions to be applied at the interface between the different phases. First we consider the interaction of the mixed phase with the solid particles. The solid phase is described by three independent variables $\tilde{\boldsymbol{u}}^s$, the mixed phase is described by four $\tilde{\boldsymbol{u}}^m$ and p^w. Hence, we need a total of 7 conditions at the interface. We assume that the total stress is continuous across the boundary

$$\hat{\boldsymbol{n}}^{ms} \cdot \tilde{\sigma}^{s,j} = \hat{\boldsymbol{n}}^{ms} \cdot \tilde{\sigma}^m - \hat{\boldsymbol{n}}^{ms} \tilde{p}^w, \qquad \boldsymbol{x} \in \Gamma_{ms}. \tag{2.6a}$$

We assume zero penetration of the mixed phase into the solid phase. Hence, the boundary condition on the solid part of the mixed phase is simply that the normal component of the displacement in the mixed phase is the same as that on the solid boundary

$$\hat{\boldsymbol{n}}^{ms} \cdot \tilde{\boldsymbol{u}}^{m} = \hat{\boldsymbol{n}}^{ms} \cdot \tilde{\boldsymbol{u}}^{s,j}, \qquad \boldsymbol{x} \in \Gamma_{ms}. \tag{2.6b}$$

In order that the fluid component of the mixed phase does not penetrate into the solid we require that the Darcy velocity normal to the interface is zero, *i.e.* the fluid and solid components of the mixed phase have the same velocity. This can be written as

$$\frac{k}{\mu^{w}} \hat{\boldsymbol{n}}^{ms} \cdot \left(\tilde{\boldsymbol{\nabla}} \tilde{p}^{w} + \rho^{w} g \hat{\boldsymbol{e}}_{3} \right) = 0, \qquad \boldsymbol{x} \in \Gamma_{ms}. \tag{2.6c}$$

This gives us 5 conditions in total. We need two more conditions to fully perscribe the behaviour on the boundary. In order to make the theory as general as possible we choose to write a standard Navier slip condition on the mixed–solid interface

$$\tilde{\boldsymbol{u}}^{m} - \tilde{\boldsymbol{u}}^{s} = -\tilde{\lambda}^{s} \hat{\boldsymbol{n}}^{ms} \cdot \tilde{e}\left(\tilde{\boldsymbol{u}}^{m}\right) \left(I - \hat{\boldsymbol{n}}^{ms} \hat{\boldsymbol{n}}^{ms} \right), \qquad \boldsymbol{x} \in \Gamma_{ms}, \tag{2.6d}$$

where $\tilde{\lambda}^{s}$ is the Navier slip length, assumed constant across all solid grains. We note that if equation (2.6*d*) is projected in the direction normal to the interface it reduces to equation (2.6*b*). Hence, we have a total of 7 equations on the mixed phase–solid interface. Similarly we write the conditions on the air–mixed phase interface as

$$\frac{k}{\mu^{w}} \hat{\boldsymbol{n}}^{am} \cdot \left(\tilde{\boldsymbol{\nabla}} \tilde{p}^{w} + \rho^{w} g \hat{\boldsymbol{e}}_{3} \right) = 0, \qquad \boldsymbol{x} \in \Gamma_{am}, \tag{2.7a}$$

$$\hat{\boldsymbol{n}}^{am} \cdot \tilde{\sigma}^{a} - \hat{\boldsymbol{n}}^{am} (\tilde{p}^{a} - \gamma\kappa) = \hat{\boldsymbol{n}}^{am} \cdot \tilde{\sigma}^{m} - \hat{\boldsymbol{n}}^{am} \tilde{p}^{w}, \qquad \boldsymbol{x} \in \Gamma_{am}, \tag{2.7b}$$

$$\tilde{\boldsymbol{v}}^{m} - \tilde{\boldsymbol{v}}^{a} = -\tilde{\lambda}^{a} \hat{\boldsymbol{n}}^{am} \cdot \overset{\circ}{\tilde{e}}\left(\tilde{\boldsymbol{u}}^{m}\right) \left(I - \hat{\boldsymbol{n}}^{am} \hat{\boldsymbol{n}}^{am} \right), \qquad \boldsymbol{x} \in \Gamma_{am}. \tag{2.7c}$$

Here κ is the mean curvature of the interface which is assumed known a-priori, γ is the surface tension and $\tilde{\lambda}^{a}$ is the Navier slip length on the air–mixed interface. As the air phase is defined in terms of a velocity $\tilde{\boldsymbol{v}}^{a}$ rather than a displacement the appropriate tensor derivative $\overset{\circ}{\tilde{e}}\left(\tilde{\boldsymbol{u}}^{m}\right)$ is the co-deformational derivative. We shall show in the forthcoming analysis that $\overset{\circ}{\tilde{e}}\left(\tilde{\boldsymbol{u}}^{m}\right)$ does not need to be calculated as these terms do not come in till higher order. Finally we write standard conditions for the continuity of stress and velocity on the air–solid interface

$$\tilde{\boldsymbol{v}}^{a} = \tilde{\boldsymbol{v}}^{s,j}, \qquad \boldsymbol{x} \in \Gamma_{as,j}, \tag{2.8a}$$

$$\hat{\boldsymbol{n}}^{as} \cdot \tilde{\sigma}^{a} - \hat{\boldsymbol{n}}^{as} \tilde{p}^{a} = \hat{\boldsymbol{n}}^{as} \cdot \tilde{\sigma}^{s,j}, \qquad \boldsymbol{x} \in \Gamma_{as,j}. \tag{2.8b}$$

These boundary conditions, when coupled with appropriate initial conditions, complete the description of the coupled mixed phase–solid–fluid system.

(b) Non-dimensional equations

In order to simplify the model and approximate the effect of each parameter we non-dimensionalise equations (2.1) using $\tilde{\boldsymbol{u}}^{r} = [\boldsymbol{u}]\boldsymbol{u}^{r}$, $\tilde{\boldsymbol{v}}^{r} = [\boldsymbol{v}]\boldsymbol{v}^{r}$, $\tilde{t} = [t]t$, $\tilde{\boldsymbol{x}} = [\boldsymbol{x}]\boldsymbol{x}$ and $\tilde{p}^{r} = [p]p^{r}$. We are interested in considering a system of typical size L_x with periodic micro-structure of length L_y. We want to obtain a model which is valid on the macroscopic length scale L_x and we non-dimensionalise with respect to this length. Our aim is now to write equations on the unit cell $Y = (0, \epsilon)^{3}$, where $\epsilon = \frac{L_y}{L_x} \ll 1$ is the scaling ratio. The unit cell is composed of a solid phase $\mathfrak{B}_s$,

an air phase $\mathfrak{B}_a$ and a mixed phase $\mathfrak{B}_m$. The phase boundaries are defined as $\partial\mathfrak{B}_{as,j}$, $\partial\mathfrak{B}_{ms,j}$ and $\partial\mathfrak{B}_{am}$ for the air–solid, mixed–solid and air–mixed boundaries respectively.

We consider the velocities of the solid and fluid parts of the mixed phase to be driven by the change in displacement per unit time, *i.e.*, $[\boldsymbol{v}] = [\boldsymbol{u}]/[t]$. On substitution into equations (2.1) we find that the only equation which contains $[t]$ is equation (2.2). Hence, we let equation (2.2) define the time scale of the system. In other words, the physics of the system, captured by equations (2.1), defines a natural and physically relevant set of scales for the movement of the mixed phase

$$[\boldsymbol{x}] = L_x, \quad [p] = \frac{G[\boldsymbol{u}]}{L_x}, \quad [t] = \frac{\mu^w L_x^2}{kG}. \tag{2.9}$$

This choice of scaling is the most general scaling possible. It does not limit us to a specific time frame or range of variables, rather, the scales and variables have been defined by the physics we have chosen to model. The first real constraint we place on the system is that the displacement is of size $[\boldsymbol{u}] = L_y$. This has been argued by some authors to be the smallest displacement for which a homogenisation theory can be useful [11]. Here we are considering a composite soil composed of rigid grains with a composite phase between them. The largest of these grains will both define L_y and limit the maximum displacement. Hence, we consider this a reasonable assumption.

In order to illustrate the typical time scale described by this model we consider the range of values of G, $[p]$, μ^w and k. We note that, in general, these numbers are measured for soils as a whole. In this paper we are applying these numbers to the mixed phase only. Hence, we would expect any values obtained to serve as a guide rather than as specific values. However, despite these assumptions the model will serve as a useful guide in understanding the poro-elastic behaviour of these systems. A recent compilation of soil stiffness experiments can be found in [31] in which typical values of G are given as $10^6\,\text{Pa} \lesssim G \lesssim 10^8\,\text{Pa}$ for 67 tests based on 21 clays and silts. Typical values for $[p]$ range from field capacity to plant wilting point $10^4\,\text{Pa} \lesssim [p] \lesssim 10^6\,\text{Pa}$ [32]. Soil permeability ranges from $k \lesssim 10^{-10}\,\text{m}^2$ for sandy soils to $k \lesssim 10^{-16}\,\text{m}^2$ for clays [33]. Assuming that the fluid in the mixed phase is water with viscosity $\mu^w \approx 10^{-3}\,\text{Pa}\,\text{s}$ this gives consolidation times for the mixed phase ranging from $[t]/(L_x^2) = 0.05[\text{s}\,\text{m}^{-2}]$ for $G = 10^8\,\text{Pa}$ and $k = 10^{-10}\,\text{m}^2$ to $[t]/(L_x^2) = 5 \times 10^6[\text{s}\,\text{m}^{-2}]\,\text{s}$ for $G = 10^6\,\text{Pa}$ and $k = 10^{-16}\,\text{m}^2$.

We see that for a mixed phase with high permeability ($k \lesssim 10^{-10}\,\text{m}^2$) the time scale for consolidation is fairly short, on the other hand, a mixed phase with low permeability ($k \lesssim 10^{-16}\,\text{m}^2$) results in a much longer time scale. In this theory the solid phase is assumed to be completely lubricated by a combination of the mixed phase and the air filled pore space. This means that the time scale associated with grain-grain interaction is neglected potentially resulting in a faster time scale than might be associated with soil consolidation. We have chosen to neglect this interaction as it adds significant complications to the theory and rather have focused on developing an understanding of how the mixed phase contributes to the macro-scale properties of the soil. For compactness of notation we will use the notation $\mathfrak{B}_s$, $\partial\mathfrak{B}_{ms}$, $\partial\mathfrak{B}_{as}$ to denote conditions applied indiscriminately on all solid particles. We will use the notation $\mathfrak{B}_{s,j}$, $\partial\mathfrak{B}_{ms,j}$, $\partial\mathfrak{B}_{as,j}$ etc for conditions and constraints applied to individual particles. This scaling results in the following set of non-dimensional equations

$$\boldsymbol{\nabla}\cdot\sigma^m - \boldsymbol{\nabla}p^w = g^w\left[\phi + \delta_2(1-\phi)\right]\hat{\boldsymbol{e}}_3, \qquad \boldsymbol{x}\in\mathfrak{B}_m, \tag{2.10a}$$

$$\boldsymbol{\nabla}\cdot\boldsymbol{v}^m = \boldsymbol{\nabla}\cdot\left(\boldsymbol{\nabla}p^w + g^w\hat{\boldsymbol{e}}_3\right), \qquad \boldsymbol{x}\in\mathfrak{B}_m, \tag{2.10b}$$

$$\sigma^m = e(\boldsymbol{u}^m) + \frac{\nu}{1-2\nu}\boldsymbol{\nabla}\cdot\boldsymbol{u}^m I, \qquad \boldsymbol{x}\in\mathfrak{B}_m, \tag{2.10c}$$

$$\frac{\partial\phi}{\partial t} + \boldsymbol{\nabla}\cdot\phi\boldsymbol{v}^w = 0, \qquad \boldsymbol{x}\in\mathfrak{B}_m, \tag{2.10d}$$

$$-\frac{\partial\phi}{\partial t} + \boldsymbol{\nabla}\cdot(1-\phi)\boldsymbol{v}^m = 0, \qquad \boldsymbol{x}\in\mathfrak{B}_m, \tag{2.10e}$$

$$\sum_{i=1}^{2}\left(\hat{\boldsymbol{\tau}}_i\cdot e(\boldsymbol{u}^s)\cdot\hat{\boldsymbol{e}}_j\right)^2=0, \qquad \boldsymbol{x}\in\mathfrak{B}_{s,j}, \tag{2.10f}$$

$$\int_{\partial\mathfrak{B}_{ms,j}}\hat{\boldsymbol{n}}^{ms}\cdot\sigma^{s,j}\,dx+\int_{\partial\mathfrak{B}_{as,j}}\hat{\boldsymbol{n}}^{as}\cdot\sigma^{s,j}\,dx=-\epsilon g^w\delta_4\int_{\mathfrak{B}_{s,j}}1\,dx\hat{\boldsymbol{e}}_3, \tag{2.10g}$$

$$\boldsymbol{\nabla}\cdot\sigma^a-\boldsymbol{\nabla}p^a=g^w\delta_3\hat{\boldsymbol{e}}_3, \qquad \boldsymbol{x}\in\mathfrak{B}_a, \tag{2.10h}$$

$$\boldsymbol{\nabla}\cdot\boldsymbol{v}^a=0, \qquad \boldsymbol{x}\in\mathfrak{B}_a, \tag{2.10i}$$

$$\sigma^a=\epsilon^2\delta_1 e(\boldsymbol{v}^a), \qquad \boldsymbol{x}\in\mathfrak{B}_a, \tag{2.10j}$$

$$\boldsymbol{v}^r=\frac{\partial\boldsymbol{u}^r}{\partial t}+\epsilon\boldsymbol{v}^r\cdot\boldsymbol{\nabla}\boldsymbol{u}^r, \tag{2.10k}$$

for $r=\{m,s,a,w\}$. We write the boundary conditions on the mixed-solid (2.6) interface as

$$\hat{\boldsymbol{n}}^{ms}\cdot\left(\boldsymbol{\nabla}p^w+g^w\hat{\boldsymbol{e}}_3\right)=0, \qquad \boldsymbol{x}\in\partial\mathfrak{B}_{ms}, \tag{2.10l}$$

$$\hat{\boldsymbol{n}}^{ms}\cdot\sigma^s=\hat{\boldsymbol{n}}^{ms}\cdot\sigma^m-\hat{\boldsymbol{n}}^{ms}p^w, \qquad \boldsymbol{x}\in\partial\mathfrak{B}_{ms}, \tag{2.10m}$$

$$\boldsymbol{u}^m-\boldsymbol{u}^s=\lambda^s\hat{\boldsymbol{n}}^{ms}\cdot e(\boldsymbol{u}^m)\left(I-\hat{\boldsymbol{n}}^{ms}\hat{\boldsymbol{n}}^{ms}\right), \qquad \boldsymbol{x}\in\partial\mathfrak{B}_{ms}. \tag{2.10n}$$

On the air–mixed phase boundary we write equations (2.7) as

$$\hat{\boldsymbol{n}}^{am}\cdot\left(\boldsymbol{\nabla}p^w+g^w\hat{\boldsymbol{e}}_3\right)=0, \qquad \boldsymbol{x}\in\partial\mathfrak{B}_{am}, \tag{2.10o}$$

$$\hat{\boldsymbol{n}}^{am}\cdot\sigma^a-\hat{\boldsymbol{n}}^{am}(p^a-p^c)=\hat{\boldsymbol{n}}^{am}\cdot\sigma^m-\hat{\boldsymbol{n}}^{am}p^w, \qquad \boldsymbol{x}\in\partial\mathfrak{B}_{am}, \tag{2.10p}$$

$$\boldsymbol{v}^m-\boldsymbol{v}^a=-\lambda^a\hat{\boldsymbol{n}}^{am}\cdot\mathring{e}(\boldsymbol{u}^m)\left(I-\hat{\boldsymbol{n}}^{am}\hat{\boldsymbol{n}}^{am}\right), \qquad \boldsymbol{x}\in\partial\mathfrak{B}_{am}. \tag{2.10q}$$

Finally on the air–solid interface we write equations (2.8) as

$$\boldsymbol{v}^a=\boldsymbol{v}^s, \qquad \boldsymbol{x}\in\partial\mathfrak{B}_{as}, \tag{2.10r}$$

$$\hat{\boldsymbol{n}}^{as}\cdot\sigma^a-\hat{\boldsymbol{n}}^{as}p^a=\hat{\boldsymbol{n}}^{as}\cdot\sigma^s, \qquad \boldsymbol{x}\in\partial\mathfrak{B}_{as}. \tag{2.10s}$$

Here the non-dimensional constants are

$$\begin{aligned}\delta_1&=\frac{\mu^a k}{\mu^w L_y^2}, & \delta_2&=\frac{\rho^m}{\rho^w}, & \delta_3&=\frac{\rho^a}{\rho^w}, & \delta_4&=\frac{\rho^s}{\rho^w},\\ g^w&=\frac{\rho^w g L_x^2}{G L_y}, & p^c&=\frac{\gamma\kappa L_x}{G L_y}, & \lambda^s&=\frac{\tilde{\lambda}^s}{L_x}, & \lambda^a&=\frac{\tilde{\lambda}^a}{L_x}.\end{aligned} \tag{2.11}$$

Here we have scaled such that the constants δ_j defined in equation (2.11) are of size $\lesssim O(1)$. We now consider the cases where this assumption breaks down. First we consider the case in which viscous forces from the air phase play a more significant role, *i.e.*, $\delta_1\gg 1$. Taking $\mu^w=10^{-3}\,\mathrm{Pa\,s}$, $\mu^a=2\times10^{-5}\,\mathrm{Pa\,s}$ and $k=10^{-10}\,\mathrm{m}^2$ we find this assumption breaks down for $L_y\lesssim 10^{-6}\,\mathrm{m}$. Physically, for a highly permeable mix phase, this means that the viscous flow of the air phase will have a more significant effect on the flow properties if the representative pore size considered is less than 1 micron. Typically, we are interested in representative geometries of the order of 1 mm so we do assume this approximation holds.

The parameters δ_2, δ_3 and δ_4 are the density ratios of the solid component of the mixed phase to the fluid component, the air phase to the water phase and the solid phase to the water phase. For all cases considered these will be $\lesssim O(1)$. The parameters g^w and p^c define the influence of gravity and capillary pressure. Here gravity is scaled to $O(1)$ and capillary pressure comes in at $O(\epsilon^{-1})$. By considering the parameters necessary for $g^w\gg 1$ and $p^c\gg 1$ we can determine the validity of this theory. Using $G=10^6\,\mathrm{Pa}$, $\rho^w=10^3\,\mathrm{kg\,m^{-3}}$, $g=9.8\,\mathrm{m\,s^{-2}}$, and $\gamma=70\times10^{-3}\,\mathrm{N\,m^{-1}}$ we find that gravitational effects become more dominant when $\epsilon^{-1}\lesssim g^w$, this is seen to occur for

$L_x \gtrsim 100$ m, a condition which is unlikely to occur. Similarly, the effect of capillary pressure would need to be moved to lower order for $\epsilon^{-1} \lesssim p^c$, this occurs when $\kappa \gg 10^7$ m^{-1}.

The remaining parameters in equation (2.11) are λ^a and λ^s. These are the dimensionless slip lengths for the mixed phase at the mixed–solid and air–mixed interfaces. If λ^j for $j = \{a, s\}$ is large then the boundary condition will behave as a slip condition. If it is small then the condition will behave as a no slip condition. Whilst it is possible to assign this constant a size in terms of powers of ϵ this would place unnecessary restrictions on the theory. Should λ^j be large or small this approximation can be made at a much later stage and, in the meantime, we can proceed keeping $\lambda^j \sim O(1)$ without loss of generality.

(c) Homogenization

We are now in a position to homogenize equations (2.10). Our aim is to start with equations (2.10) that are valid on the pore scale geometry, and to approximate them with a set of averaged equations that do not take into account the precise details of the geometry. These details will be captured through a set of representative cell problems which are solved on a single period of the underlying geometry. In this section, we provide a description of the steps and the key equations which result from the procedure. The mathematical steps involved in this derivation are included in the supplementary material S1. The starting point is to observe that there are two very different length scales present L_x, the macro-scale, and L_y the micro-scale. Any order 1 change on the length scale L_x will result in a change of size ϵ on the scale L_y; we will use this as the basis for an asymptotic expansion. In order to formalise this we will assume that all dependent variables are a function of both the small scale $\boldsymbol{y}$ and the large scale $\boldsymbol{x}$. In addition we follow Lee and Mei [11] and write the arbitrary field f as $f(\boldsymbol{x}) = f(\boldsymbol{x} + \boldsymbol{u}(\boldsymbol{x}), \boldsymbol{y})$, where $\boldsymbol{u}$ is the displacement vector. Expanding the spatial derivative using the chain rule we obtain

$$\boldsymbol{\nabla} = \epsilon^{-1} \boldsymbol{\nabla}_y + \left[(\boldsymbol{\nabla}_x \boldsymbol{u}) \boldsymbol{\nabla}_y + \boldsymbol{\nabla}_x \right]. \tag{2.12}$$

Here $\boldsymbol{\nabla}_x$ is the gradient operator on the macro-scale and $\boldsymbol{\nabla}_y$ is the gradient opperator on the micro-scale. The term $(\boldsymbol{\nabla}_x \boldsymbol{u}) \boldsymbol{\nabla}_y$ in equation (2.12) comes from the distortion of the medium due to elastic deformations. Using equation (2.12) we can write the strain as $e(\boldsymbol{v}) = \epsilon^{-1} e_y(\boldsymbol{v}) + e_x(\boldsymbol{v}) + e_u(\boldsymbol{v})$ where

$$e_x(\boldsymbol{v}) = (\boldsymbol{\nabla}_x \boldsymbol{v}) + (\boldsymbol{\nabla}_x \boldsymbol{v})^T, \tag{2.13}$$

$$e_y(\boldsymbol{v}) = (\boldsymbol{\nabla}_y \boldsymbol{v}) + (\boldsymbol{\nabla}_y \boldsymbol{v})^T, \tag{2.14}$$

$$e_u(\boldsymbol{v}) = \left[(\boldsymbol{\nabla}_x \boldsymbol{u}) \boldsymbol{\nabla}_y \boldsymbol{v} \right] + \left[(\boldsymbol{\nabla}_x \boldsymbol{u}) \boldsymbol{\nabla}_y \boldsymbol{v} \right]^T. \tag{2.15}$$

The final, nonlinear strain term comes from the nonlinear derivative in equation (2.12). To proceed we make the expansions

$$\boldsymbol{u}^m = \sum_{k=0}^{\infty} \epsilon^k \boldsymbol{u}_k^m, \quad \boldsymbol{u}^s = \sum_{k=0}^{\infty} \epsilon^k \boldsymbol{u}_k^s, \quad \boldsymbol{v}^a = \sum_{k=0}^{\infty} \epsilon^k \boldsymbol{v}_k^a, \quad p^w = \sum_{k=0}^{\infty} \epsilon^k p_k^w, \quad p^a = \sum_{k=0}^{\infty} \epsilon^k p_k^a. \tag{2.16}$$

In order to account for the moving geometry on the microscale we perturb the surface normals [10,24]

$$\hat{\boldsymbol{n}}^\alpha = \hat{\boldsymbol{n}}_0^\alpha + \epsilon \boldsymbol{n}_1^\alpha + O(\epsilon^2) \tag{2.17}$$

where $\alpha = \{ms, am, as\}$. The influence of the non-linear terms in equation (2.12) and the perturbed surface normals will be considered in detail in the supplementary material S1.

We proceed by substituting equations (2.16) and (2.12) into equations (2.10) and collect terms in powers of ϵ. Typically, homogenisation problems have the same structure. At $O(\epsilon^{-2})$ we find that the quantities of interest are approximately independent of the micro-scale geometry. Clearly, this

is a poor approximation and not particularly useful in its own right. Hence, we expand to $O(\epsilon^{-1})$ to determine how the first order correction to each variable depends on the micro-scale geometry. Finally, expanding to $O(\epsilon^0)$ we find a set of macro-scale equations that must be satisfied. These equations are parameterised by a set of effective properties, which depend on the first order correction to the variables. In this way the micro-scale geometry is captured in the macro-scale equations. In the case of equations (2.10) the $O(\epsilon^{-2})$ expansion is given in equations (S1.7). These have solution $\sigma_0^m = 0$, $\sigma_0^s = 0$, $\boldsymbol{u}_0^m = \boldsymbol{u}_0^m(\boldsymbol{x}, t)$, $p_0^w = p_0^w(\boldsymbol{x}, t)$, $p_0^a = p_0^a(\boldsymbol{x}, t)$ and, hence

$$\boldsymbol{v}_0^\alpha = \frac{\partial \boldsymbol{u}_0^\alpha}{\partial t}, \tag{2.18}$$

for $\alpha = \{m, s\}$. Physically this tells us that the dominant part of the displacement vectors, velocities and pressures are constant on the mico-scale. From this point on we shall write the leading order displacement and velocities in terms of the mixed phase displacement, *i.e.*, $\boldsymbol{u}_0^m$ and $\frac{\partial \boldsymbol{u}_0^m}{\partial t}$.

(i) Cell problems

Collecting terms at $O(\epsilon^{-1})$ and using results from $O(\epsilon^{-2})$ we obtain a set of independent cell problems for $\boldsymbol{u}_1^m$, p_1^w, p_1^a and $\boldsymbol{v}_0^a$. Typically, at this stage of the homogenisation procedure two steps are taken. The first is to check the compatibility of the equations with the boundary conditions, *i.e.*, checking for solvability. The second step is to simplify these equations so that a cell problem can be solved on a representative geometry. This amounts to factoring the large scale dependencies out of the equations, see supplementary material S1 for details. The first of these is the $O(\epsilon^{-1})$ expansion for p_1^a and $\boldsymbol{v}_0^a$, which is given in equations (S1.9). These equations describe the local air velocity driven by macro-scale pressure gradients in the air phase and movement of the adjacent mixed phase. This type of equation is standard in the homogenisation literature [20], hence, we do not show solvability. Equations (S1.9) have the solution

$$\boldsymbol{v}_0^a = \frac{\partial \boldsymbol{u}_0^m}{\partial t} + \frac{1}{\delta_1} \sum_{k=1}^{3} \boldsymbol{\zeta}_k \hat{\boldsymbol{e}}_k \cdot \left(\boldsymbol{\nabla}_x p_0^a + g^w \delta_3 \hat{\boldsymbol{e}}_3 \right), \quad p_1^a = \sum_{k=1}^{3} \omega_k^a \hat{\boldsymbol{e}}_k \cdot \left(\boldsymbol{\nabla}_x p_0^a + g^w \delta_3 \hat{\boldsymbol{e}}_3 \right), \tag{2.19}$$

where $\boldsymbol{\zeta}_k$ and ω_k^a satisfy the cell problem

$$\nabla_y^2 \boldsymbol{\zeta}_k - \boldsymbol{\nabla}_y \omega_k^a = \hat{\boldsymbol{e}}_k, \qquad \boldsymbol{y} \in \mathfrak{B}_a, \tag{2.20a}$$

$$\boldsymbol{\nabla}_y \cdot \boldsymbol{\zeta}_k = 0, \qquad \boldsymbol{y} \in \mathfrak{B}_a, \tag{2.20b}$$

$$\boldsymbol{\zeta}_k = 0, \qquad \boldsymbol{y} \in \partial\mathfrak{B}_{as} \cup \partial\mathfrak{B}_{am}. \tag{2.20c}$$

The second cell problem describes the local movement of water within the mixed phase. On the micro-scale this movement is described by Darcy flow driven by macro-scale pressure gradients in the mixed phase, see equations (S1.12). Again, this type of problem is standard in the homogenisation literature [34], hence, we do not show solvability. Equations (S1.12) have the solution

$$p_1^w = \sum_{k=1}^{3} \omega_k^w \hat{\boldsymbol{e}}_k \cdot \left(\boldsymbol{\nabla}_x p_0^w + g^w \hat{\boldsymbol{e}}_3 \right), \tag{2.21}$$

where ω_k^w satisfies the cell problem

$$\nabla_y^2 \omega_k^w = 0, \qquad \boldsymbol{y} \in \mathfrak{B}_m, \tag{2.22a}$$

$$\hat{\boldsymbol{n}}_0^{ms} \cdot \boldsymbol{\nabla}_y \omega_k^w + \hat{\boldsymbol{n}}_0^{ms} \cdot \hat{\boldsymbol{e}}_k = 0, \qquad \boldsymbol{y} \in \partial\mathfrak{B}_{ms}, \tag{2.22b}$$

$$\hat{\boldsymbol{n}}_0^{am} \cdot \boldsymbol{\nabla}_y \omega_k^w + \hat{\boldsymbol{n}}_0^{am} \cdot \hat{\boldsymbol{e}}_k = 0, \qquad \boldsymbol{y} \in \partial\mathfrak{B}_{am}. \tag{2.22c}$$

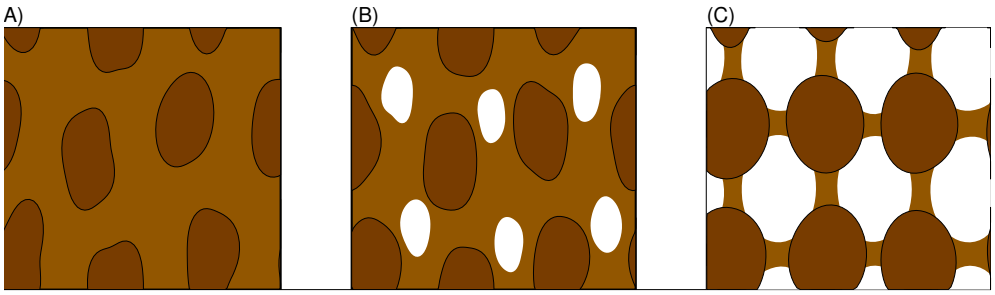

Figure 2. Schematic showing the solvability condition for three cases (A) no air, (B) isolated air pockets, and (C) balanced air pockets such that equation (2.23) is satisfied.

The remaining two cell problems come from the expansion of the constitutive equations in the mixed phase. The expansion is given in equations (S1.15). Unlike equations (S1.9) and (S1.12), solvability of equations (S1.15) is not guaranteed. On inspection we find that the solvability condition, which the representative geometry must satisfy, is

$$\int_{\partial \mathfrak{B}_{am}} \hat{\boldsymbol{n}}_0^{am} p^c \, d\boldsymbol{y} = 0. \tag{2.23}$$

This condition can be interpreted as a statement of mechanical equilibrium. It states that the total force on the disconnected particles must be zero. We note that this is the total force on all solid particles not on an individual solid particle. There are several ways in which this condition can be met, these are illustrated in figure 2. The first way this condition can be met is simply if there is no air present in the soil, see figure 2A. Secondly, if the solid particle surface is completely wetted then the air–mixed phase interface will form a closed surface. Hence, the integral in equation (2.23) will be automatically zero, see figure 2B. Finally, if the air–mixed phase interface is naturally arranged such that all contributions from the capillary pressure cancel out, see figure 2C.

This theory describes perturbations about a steady state, hence, for any real geometry we would expect that this condition is naturally met. However, from a practical point of view this theory could be applied to a geometry obtained via X-CT imaging. It is likely that, due to imaging artefacts, this condition will not be satisfied. Hence, in order to ensure that the cell problems obtained from equations (S1.15) have a solution we introduce the normalised error

$$\boldsymbol{E} = \frac{1}{||\partial \mathfrak{B}_{am}||} \int_{\partial \mathfrak{B}_{am}} \hat{\boldsymbol{n}}_0^{am} \, d\boldsymbol{y}. \tag{2.24}$$

where for an arbitrary domain ξ we define

$$||\xi|| = \int_{\xi} 1 \, d\boldsymbol{y}. \tag{2.25}$$

Hence, we find equations (S1.15) have the solution

$$\boldsymbol{u}_1^m = \sum_{p=1,q=1}^{3} \boldsymbol{\kappa}_{pq}^u \hat{\boldsymbol{e}}_p \cdot e_x(\boldsymbol{u}_0^m) \cdot \hat{\boldsymbol{e}}_q + \boldsymbol{\kappa}^p \left(p_0^w + p^c - p_0^a\right), \tag{2.26}$$

$$\boldsymbol{u}_1^s = \sum_{p=1,q=1}^{3} \boldsymbol{\gamma}_{pq}^u \hat{\boldsymbol{e}}_p \cdot e_x(\boldsymbol{u}_0^m) \cdot \hat{\boldsymbol{e}}_q + \boldsymbol{\gamma}^p \left(p_0^w + p^c - p_0^a\right), \tag{2.27}$$

where $\boldsymbol{\kappa}^u_{pq}$ and $\boldsymbol{\gamma}^u_{pq}$ satisfy

$$\boldsymbol{\nabla}_y \cdot \alpha^u_{pq} = 0, \qquad \boldsymbol{y} \in \mathfrak{B}_m, \tag{2.28a}$$

$$\alpha^u_{pq} = e_y(\boldsymbol{\kappa}^u_{pq}) + \frac{\nu}{1-2\nu}\left(\boldsymbol{\nabla}_y \cdot \boldsymbol{\kappa}^u_{pq}\right) I, \qquad \boldsymbol{y} \in \mathfrak{B}_m, \tag{2.28b}$$

$$\sum_{i=1}^{2}\left[\hat{\boldsymbol{\tau}}_i \cdot e_y(\boldsymbol{\gamma}^u_{pq}) \cdot \hat{\boldsymbol{e}}_j + \hat{\boldsymbol{\tau}}_i \cdot \frac{1}{2}\left(\hat{\boldsymbol{e}}_p\hat{\boldsymbol{e}}_q + \hat{\boldsymbol{e}}_q\hat{\boldsymbol{e}}_p\right) \cdot \hat{\boldsymbol{e}}_j\right]^2 = 0, \qquad \boldsymbol{y} \in \partial\mathfrak{B}_s, \tag{2.28c}$$

$$\int_{\partial\mathfrak{B}_{ms,j}} \hat{\boldsymbol{n}}^{ms}_0 \cdot \alpha^u_{pq}|_j \, d\boldsymbol{y} = 0, \tag{2.28d}$$

$$\boldsymbol{\kappa}^u_{pq} - \boldsymbol{\gamma}^u_{pq} = \lambda^s \hat{\boldsymbol{n}}^{ms}_0 \left[e_y(\boldsymbol{\kappa}^u_{pq}) + \hat{\boldsymbol{e}}_p\hat{\boldsymbol{e}}_q\right]\left[I - \hat{\boldsymbol{n}}^{ms}_0\hat{\boldsymbol{n}}^{ms}_0\right], \qquad \boldsymbol{y} \in \partial\mathfrak{B}_{ms}, \tag{2.28e}$$

$$\hat{\boldsymbol{n}}^{am}_0 \cdot \left[\alpha^u_{pq} + \hat{\boldsymbol{e}}_p\hat{\boldsymbol{e}}_q + \frac{\nu}{1-2\nu}\frac{\hat{\boldsymbol{e}}_p \cdot \hat{\boldsymbol{e}}_q}{2}\right] = 0, \qquad \boldsymbol{y} \in \partial\mathfrak{B}_{am}, \tag{2.28f}$$

and $\boldsymbol{\kappa}^p$ and $\boldsymbol{\gamma}^p$ satisfy

$$\boldsymbol{\nabla}_y \cdot \alpha^p = 0, \qquad \boldsymbol{y} \in \mathfrak{B}_m, \tag{2.29a}$$

$$\alpha^p = e_y(\boldsymbol{\kappa^p}) + \frac{\nu}{1-2\nu}\left(\boldsymbol{\nabla}_y \cdot \boldsymbol{\kappa}^p\right) I, \qquad \boldsymbol{y} \in \mathfrak{B}_m, \tag{2.29b}$$

$$\sum_{i=1}^{2}\left(\hat{\boldsymbol{\tau}}_i \cdot e_y(\boldsymbol{\gamma^p}) \cdot \hat{\boldsymbol{e}}_j\right)^2 = 0, \qquad \boldsymbol{y} \in \partial\mathfrak{B}_s, \tag{2.29c}$$

$$\int_{\partial\mathfrak{B}_{ms,j}} \hat{\boldsymbol{n}}^{ms}_0 \cdot \alpha^p \, d\boldsymbol{y} = 0, \tag{2.29d}$$

$$\boldsymbol{\kappa}^p - \boldsymbol{\gamma}^p = \lambda^s \hat{\boldsymbol{n}}^{ms}_0 e_y(\boldsymbol{\kappa}^p)\left[I - \hat{\boldsymbol{n}}^{ms}_0\hat{\boldsymbol{n}}^{ms}_0\right], \qquad \boldsymbol{y} \in \partial\mathfrak{B}_{ms}, \tag{2.29e}$$

$$\hat{\boldsymbol{n}}^{am}_0 \cdot \alpha^p = \hat{\boldsymbol{n}}^{am}_0 - \boldsymbol{E}, \qquad \boldsymbol{y} \in \partial\mathfrak{B}_{am}, \tag{2.29f}$$

where we have added the normalised error to equation (2.29*f*) to ensure that the cell problem (2.29) is well posed. From a physical perspective cell problems (2.28) and (2.29) describe the resistance to deformation by macro-scale strain and pressure offered by the micro-scale geometry. Finally, we obtain the velocity expansion at $O(\epsilon^{-1})$:

$$\boldsymbol{v}^\alpha_1 = \frac{\partial \boldsymbol{u}^\alpha_1}{\partial t} + \frac{\partial \boldsymbol{u}^m_0}{\partial t} \cdot \left[\boldsymbol{\nabla}_y \boldsymbol{u}^\alpha_1 + \boldsymbol{\nabla}_x \boldsymbol{u}^\alpha_0\right], \tag{2.30}$$

for $\alpha = \{m, s, a, w\}$; we will use equation (2.30) at $O(\epsilon^0)$. Equations (2.20), (2.22), (2.28) and (2.29) capture the effect of the micro-scale geometry. This information will be used at higher order to obtain an averaged set of equations which describe the poro-elastic material as a continuum.

(ii) Averaged equations

The final stage in the homogenisation procedure is to expand equations (2.10) to $O(\epsilon^0)$ and, as at the previous order, find the conditions under which the resulting equations have a solution. The result is a set of macro-scale equations which depend on the cell problems (2.20), (2.22), (2.28), and (2.29). The expansion to $O(\epsilon^0)$ is given in (S1.27). To check for solvability and, hence, obtain the macroscopic equations averaged over the micro-scale we integrate equations (S1.27*a*), (S1.27*b*) and (S1.27*d*) in turn. This step involves a significant amount of non-trivial algebra, the details of which are included in the supplementary material S1. For compactness, we present the results here. The macro-scale force balance is given by

$$\left[\frac{\partial}{\partial x_i}C^u_{ijkl}+\frac{\partial u^m_{0p}}{\partial x_i}\mathcal{H}^u_{ijklp}\right]\left[\frac{\partial u^m_{0k}}{\partial x_l}+\frac{\partial u^m_{0l}}{\partial x_k}\right]+\left[\frac{\partial}{\partial x_i}C^p_{ij}+\frac{\partial u^m_{0p}}{\partial x_i}\mathcal{H}^p_{ijp}\right](p^w_0+p^c-p^a_0)$$
$$-\frac{\partial}{\partial x_i}\left[\left(||\mathcal{B}_m||\delta_{ij}-\int_{\partial\mathfrak{B}_{ms}}\hat{n}^{ms}_{0j}y_i\,dy\right)p^w_0+\left(||\mathcal{B}_a||\delta_{ij}-\int_{\partial\mathfrak{B}_{as}}\hat{n}^{as}_{0j}y_i\,dy\right)p^a_0\right]=g^{eff}\hat{\boldsymbol{e}}_3, \tag{2.31}$$

where C^u_{ijkl} and $\mathcal{H}^u_{ijklp}$ are the coefficients of the linear and non-linear parts of the stiffness tensors, C^p_{ij} and $\mathcal{H}^p_{ijp}$ are the coefficients of the linear and non-linear pressure induced stress and G^{eff} is the effective gravitational force. The non-linear terms in equation (2.31) come from the additional terms in the gradient operator, equation (2.12). The effective parameters, defined through the cell problems, are given by

$$\begin{aligned}C^u_{ijkl}=&\int_{\mathfrak{B}_m}\left[\frac{\partial\kappa^u_{kli}}{\partial y_j}+\frac{\partial\kappa^u_{klj}}{\partial y_i}+\delta_{ik}\delta_{jl}+\frac{\nu}{1-2\nu}\left(\delta_{ij}\delta_{kl}+\boldsymbol{\nabla}_y\cdot\boldsymbol{\kappa}^u_{kl}\delta_{ij}\right)\right]d\boldsymbol{y}\\&-\int_{\partial\mathfrak{B}_{ms}}y_i\hat{n}^{ms}_{0q}\left[\frac{\partial\kappa^u_{klq}}{\partial y_j}+\frac{\partial\kappa^u_{klj}}{\partial y_q}+\delta_{qk}\delta_{jl}+\frac{\nu}{1-2\nu}\left(\delta_{qj}\delta_{kl}+\boldsymbol{\nabla}_y\cdot\boldsymbol{\kappa}^u_{kl}\delta_{qj}\right)\right]d\boldsymbol{y},\end{aligned} \tag{2.32a}$$

$$\mathcal{H}^u_{ijklp}=\int_{\mathfrak{B}_m}\frac{\partial}{\partial y_p}\left[\frac{\partial\kappa^u_{kli}}{\partial y_j}+\frac{\partial\kappa^u_{klj}}{\partial y_i}+\frac{\nu}{1-2\nu}\boldsymbol{\nabla}_y\cdot\boldsymbol{\kappa}^u_{kl}\delta_{ij}\right]d\boldsymbol{y}, \tag{2.32b}$$

$$\begin{aligned}C^p_{ij}=&\int_{\mathfrak{B}_m}\left[\frac{\partial\kappa^p_i}{\partial y_j}+\frac{\partial\kappa^p_j}{\partial y_i}+\frac{\nu}{1-2\nu}\boldsymbol{\nabla}_y\cdot\boldsymbol{\kappa}^p\delta_{ij}\right]d\boldsymbol{y}\\&-\int_{\partial\mathfrak{B}_{ms}}y_i\hat{n}^{ms}_{0q}\left[\frac{\partial\kappa^p_q}{\partial y_j}+\frac{\partial\kappa^p_j}{\partial y_q}+\frac{\nu}{1-2\nu}\boldsymbol{\nabla}_y\cdot\boldsymbol{\kappa}^p\delta_{qj}\right]d\boldsymbol{y},\end{aligned} \tag{2.32c}$$

$$\mathcal{H}^p_{ijp}=\int_{\mathfrak{B}_m}\frac{\partial}{\partial y_p}\left[\frac{\partial\kappa^p_i}{\partial y_j}+\frac{\partial\kappa^p_j}{\partial y_i}+\frac{\nu}{1-2\nu}\boldsymbol{\nabla}_y\cdot\boldsymbol{\kappa}^p\delta_{ij}\right]d\boldsymbol{y}, \tag{2.32d}$$

and

$$g^{eff}=g^w\left\{||\mathfrak{B}_m||\left[\phi+\delta_2(1-\phi)\right]+||\mathfrak{B}_a||\delta_3+||\mathfrak{B}_s||\delta_4\right\}. \tag{2.32e}$$

The effective equation for water movement, derived in the supplementary material S1, is

$$\begin{aligned}&||\mathfrak{B}_m||\frac{\partial^2u^m_{0j}}{\partial t\partial x_j}+A^u_{pq}\frac{\partial}{\partial t}\left[\frac{\partial u^m_{0p}}{\partial x_q}+\frac{\partial u^m_{0q}}{\partial x_p}\right]+A^p\frac{\partial}{\partial t}\left(p^c+p^w_0-p^a_0\right)\\&+\frac{\partial u^m_{0i}}{\partial t}\left\{\mathcal{A}^u_{ipq}\left[\frac{\partial u^m_{0p}}{\partial x_q}+\frac{\partial u^m_{0q}}{\partial x_p}\right]+\mathcal{A}^p_i\left(p^c+p^w_0-p^a_0\right)\right\}\\&=\left[\frac{\partial}{\partial x_j}K^w_{jk}+\frac{\partial u^m_{0i}}{\partial x_j}\mathcal{K}^w_{ijk}\right]\left[\frac{\partial p^w_0}{\partial x_k}+g^w\delta_{k3}\right],\end{aligned} \tag{2.33}$$

where K^w_{ij} and $\mathcal{K}^w_{ijk}$ are the effective water mobilities, A^u_{pq} and $\mathcal{A}^u_{ipq}$ are the strain induced variations in water content, and A^p and $\mathcal{A}^p_i$ are the pressure induced variations in water content. These effective parameters are given by

$$\begin{aligned}&K^w_{ij}=\int_{\mathfrak{B}_m}\delta_{ij}+\frac{\partial\omega_j}{\partial y_i}\,d\boldsymbol{y},\quad A^u_{pq}=\int_{\mathfrak{B}_m}\boldsymbol{\nabla}_y\cdot\boldsymbol{\kappa}^u_{pq}\,d\boldsymbol{y},\quad A^p=\int_{\mathfrak{B}_m}\boldsymbol{\nabla}_y\cdot\boldsymbol{\kappa}^p\,d\boldsymbol{y},\\&\mathcal{K}^w_{ijk}=\int_{\mathfrak{B}_m}\frac{\partial^2\omega^w_k}{\partial y_i\partial y_j}\,d\boldsymbol{y},\quad\mathcal{A}^u_{ipq}=\int_{\mathfrak{B}_m}\frac{\partial}{\partial y_i}\boldsymbol{\nabla}_y\cdot\boldsymbol{\kappa}^u_{pq}\,d\boldsymbol{y},\quad\mathcal{A}^p_i=\int_{\mathfrak{B}_m}\frac{\partial}{\partial y_i}\boldsymbol{\nabla}_y\cdot\boldsymbol{\kappa}^p\,d\boldsymbol{y}.\end{aligned} \tag{2.34}$$

Finally, the effective equation for air movement, derived in the supplementary material S1, is

$$
\begin{aligned}
&||\mathfrak{B}_a||\frac{\partial^2 \boldsymbol{u}_{0j}^m}{\partial t \partial x_j} + B_{pq}^u \frac{\partial}{\partial t}\left[\frac{\partial u_{0p}^m}{\partial x_q} + \frac{\partial u_{0q}^m}{\partial x_p}\right] + B^p \frac{\partial}{\partial t}\left(p^c + p_0^w - p_0^a\right) \\
&+\frac{\partial u_{0i}^m}{\partial t}\left\{\mathcal{B}_{ipq}^u\left[\frac{\partial u_{0p}^m}{\partial x_q} + \frac{\partial u_{0q}^m}{\partial x_p}\right] + \mathcal{B}_i^p\left(p^c + p_0^w - p_0^a\right)\right\} \\
&= -\left[\frac{\partial}{\partial x_j} K_{jk}^a + \frac{\partial u_{0i}^m}{\partial x_j}\mathcal{K}_{ijk}^a\right]\left[\frac{\partial p_0^a}{\partial x_k} + g^w \delta_3 \delta_{k3}\right],
\end{aligned}
\tag{2.35}
$$

where K_{ij}^a and $\mathcal{K}_{ijk}^a$ are the effective air mobilities, B_{pq}^u and $\mathcal{B}_{ipq}^u$ are the strain induced variations in air content, and B^p and $\mathcal{B}_i^p$ are the pressure induced variations in air content.

$$K_{ij}^a = \frac{1}{\delta_1}\int_{\mathfrak{B}_a} \boldsymbol{\zeta}_i \cdot \hat{\boldsymbol{e}}_j \, d\boldsymbol{y}, \tag{2.36a}$$

$$\mathcal{K}_{ijk}^a = \frac{1}{\delta_1}\int_{\mathfrak{B}_a} \frac{\partial \zeta_{kj}}{\partial y_i} \, d\boldsymbol{y}, \tag{2.36b}$$

$$B_{pq}^u = \int_{\partial \mathfrak{B}_{am}} \hat{\boldsymbol{n}}_0^{am} \cdot \boldsymbol{\kappa}_{pq}^u \, d\boldsymbol{y} + \sum_j \int_{\partial \mathfrak{B}_{as,j}} \hat{\boldsymbol{n}}_0^{am} \cdot \boldsymbol{\gamma}_{pq}^u \, d\boldsymbol{y}, \tag{2.36c}$$

$$\mathcal{B}_{ipq}^u = \int_{\partial \mathfrak{B}_{am}} \frac{\partial}{\partial y_i}\hat{\boldsymbol{n}}_0^{am} \cdot \boldsymbol{\kappa}_{pq}^u \, d\boldsymbol{y} + \sum_j \int_{\partial \mathfrak{B}_{as,j}} \frac{\partial}{\partial y_i}\hat{\boldsymbol{n}}_0^{am} \cdot \boldsymbol{\gamma}_{pq}^u \, d\boldsymbol{y}, \tag{2.36d}$$

$$B^p = \int_{\partial \mathfrak{B}_{am}} \hat{\boldsymbol{n}}_0^{am} \cdot \boldsymbol{\kappa}^p \, d\boldsymbol{y} + \sum_j \int_{\partial \mathfrak{B}_{as,j}} \hat{\boldsymbol{n}}_0^{am} \cdot \boldsymbol{\gamma}^p \, d\boldsymbol{y}, \tag{2.36e}$$

$$\mathcal{B}_i^p = \int_{\partial \mathfrak{B}_{am}} \frac{\partial}{\partial y_i}\left(\hat{\boldsymbol{n}}_0^{am} \cdot \boldsymbol{\kappa}^p\right) \, d\boldsymbol{y} + \sum_j \int_{\Gamma_{as,j}} \frac{\partial}{\partial y_i}\left(\hat{\boldsymbol{n}}_0^{am} \cdot \boldsymbol{\gamma}^p\right) \, d\boldsymbol{y}. \tag{2.36f}$$

(2.36g)

In summary we have found three averaged equations (2.33), (2.31) and (2.35) for p_0^a, p_0^w and $\boldsymbol{u}_0^m$. These equations are parametrised by 16 tensor and scalar quantities (2.34), (**??**) and (2.36), which are based on the 4 cell problems (2.20), (2.22), (2.28) and (2.29). The input to the cell problems consists of a reference geometry and the drained Poisson ratio for the mixed phase. The dimensionless parameters can be derived directly from the cell problems; if the air phase is connected then δ_1 is also required to parameterise equation (2.35). This is dependent on the physical air and water viscosity, and the permeability of the mixed phase. In addition the relative effect of gravity on each phase is captured through 3 parameters based on the micro-scale geometry.

3. Validation of the homogenisation procedure

We validate the homogenised equations through comparison of the governing equations (2.10) to the homogenised equations (2.33), (2.31) and (2.35). Our aim is to test the validity of the mathematical steps that we have taken in deriving (2.33), (2.31), and (2.35) from (2.10). We emphasise that this validation does not guarantee the accuracy of the underlying equations (2.10). We consider two different cases based on typical characterisation methods for elastic materials, the confined compression test [35], and the simple shear test, figure 3.

In the confined compression test a displacement is applied to the composite in the vertical direction whilst the material is constrained in the lateral directions to prevent barreling. As a result any compression can only occur in the vertical direction. The displacement is increased linearly in time until a given value is reached. The force required to make this displacement is measured as a function of time. Typically the force will increase with the displacement. Once the displacement stops increasing the material will relax and the force will decrease to a steady value. The relaxation dynamics is a function of the permeability. The steady state force is a function of the shear modulus and poisson ratio. Hence, the force output by this test represents a good

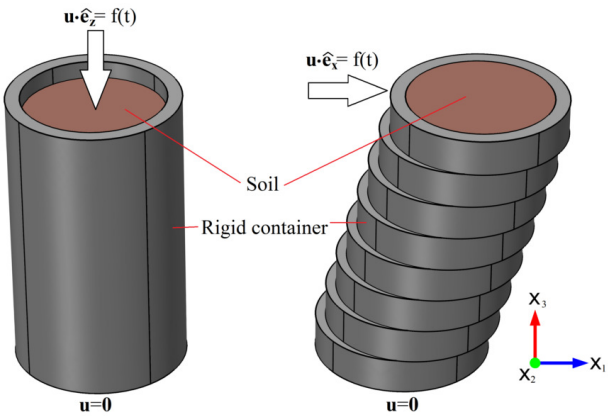

Figure 3. Illustration of confined compression test (left) and simple shear test (right).

way to validate all the homogenised parameters. The second test we consider is a simple shear experiment. The top of the material is displaced linearly in time in the horizontal direction. The material is constrained at the base inducing a shear stress. This stress is dependent only on the effective shear modulus of the material. Hence, in combination with the confined compression test this would allow us to characterise a linear poro-elastic material. Here, the combination of these tests will allow us to validate the homogenisation theory.

We consider the geometry shown in figure 4. This geometry consists of a periodic array of solid particles and air bubbles. The solid particles have dimensionless radius r_s and the air bubbles have dimensionless radius r_a. We will use these parameters as control variables in order to validate the homogenised equations for a series of different pore space geometries. Typically the homogenised equations will converge once the number of representative cells becomes sufficiently large, *i.e.*, $L_y/L_x = \epsilon \ll 1$. In this case we have found that the problems converge nicely for as few as 4 repetitions of the unit volume. However, to illustrate the use of this method, we present results just for the case in which the representative volume is composed of 8 repetitions of the representative cell.

We now test the homogenised equations for particles of varying size by comparing the governing equations to the homogenised equations (2.33), (2.31) and (2.35). We consider a composite material which has a periodic micro–structure, see Figure 4. The material is assumed to extend infinitely in the x_1 and x_2 directions. On the top surface we apply a compression in the x_3 direction of the form

$$\hat{\boldsymbol{e}}_3 \cdot \boldsymbol{u}_0^m = \begin{cases} -0.1t & t < 0.05 \\ 0.005 & t \geq 0.05 \end{cases} . \tag{3.1}$$

On the bottom of the geometry we assumed zero displacement, $\boldsymbol{u}_0^m = 0$, and used periodic boundary conditions on the sides of the geometry such that the total simulated geometry is a 1 by 8 array of solid particles contained within the mixed phase. Similarly for the shear test we apply a force of the form

$$\hat{\boldsymbol{e}}_1 \cdot \boldsymbol{u}_0^m = \begin{cases} -0.1t & t < 0.05 \\ 0.005 & t \geq 0.05 \end{cases} \tag{3.2}$$

on the top of the geometry. The remaining conditions are the same as for the confined compression case.

Previously, it has been shown that for isotropic geometries the non-linear terms associated with poro-elastic problems are zero [11]. We have confirmed through numerical simulation that, for our geometry, this is the case for the parameters $\mathcal{H}^u_{ijklp}$, $\mathcal{A}^u_{pq}$, $\mathcal{A}^p$, $\mathcal{H}^p_{ijp}$ and $\mathcal{K}^w_{ijk}$. The remaining

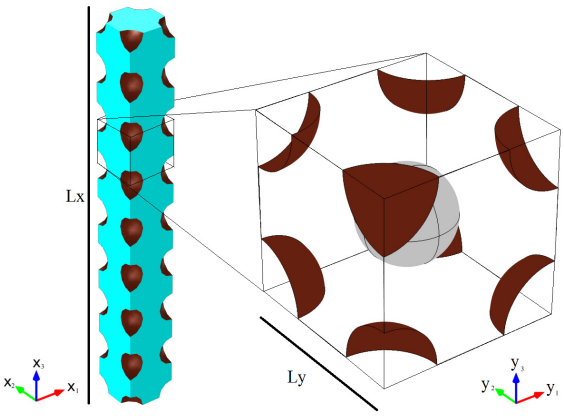

Figure 4. The geometry used to validate homogenised equations (left). A stack of solid and air filled spheres is used to solve the full equations for a variety of different sized spheres. The geometry is infinitely extended in the x_1 and x_2 directions and is composed of repeated translations of the unit cell (right). The cell problems are solved on a single unit cell at steady state. For the mechanical tests considered here the homogenised equation reduces to a one dimensional problem.

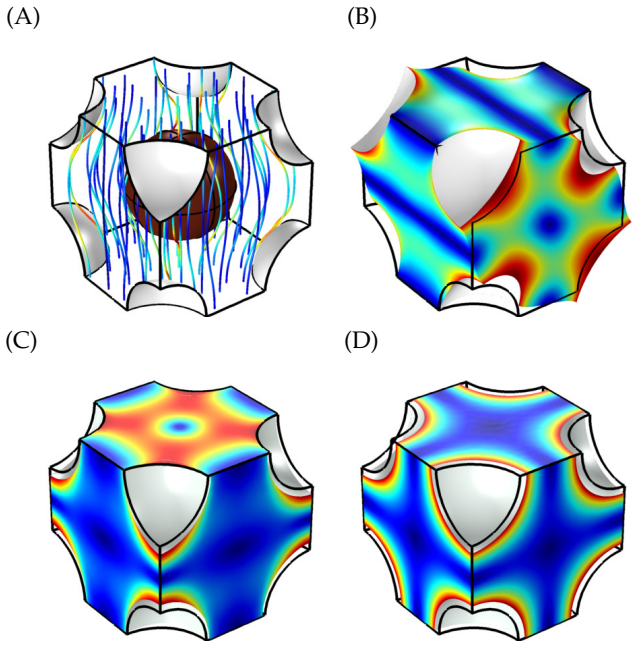

Figure 5. Example to cell problems for $r_a = 0.3$ and $r_s = 0.3$. (A) shows the microscale flow pathways taken by the water phase, *i.e.*, the solution to equations (2.20). (B),(C) and (D) show the displaced geometry due to shear (B), compression (C) and pressure (D). The color shows the modulus of displacement with red corresponding to large displacement and blue to small displacement.

effective parameters are derived by solving the cell problems on the representative geometry shown in figure 4.

We consider the time dynamics of the confined compression and simple shear test. We solve equations (2.20), (2.22), (2.28) and (2.29) numerically to determine the effective parameters in equations (2.33), (2.31) and (2.35). We solved cell problems for solid spheres of radius $r_s = 0.1$

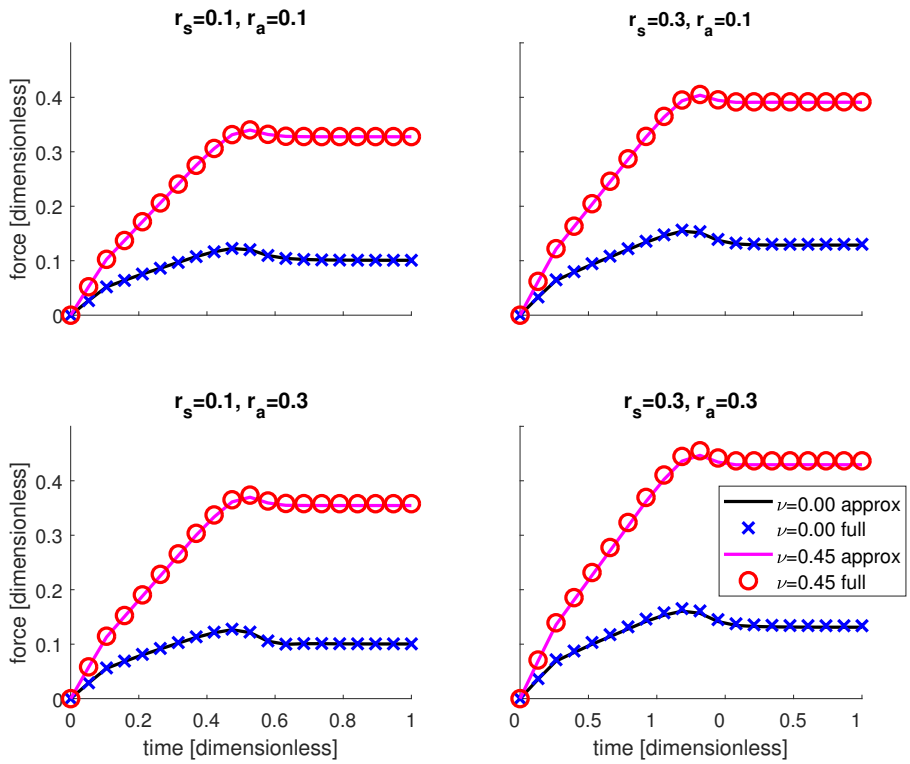

Figure 6. Validation of homogenised equations in confined compression test. The plots show the force measured due to a ramped displacement of the form given in equation (3.1).

and $r_s = 0.3$, air bubbles of radius $r_a = 0.1$ and $r_a = 0.3$. We have considered two different cases; Poisson ratio of $\nu = 0.00$ and $\nu = 0.45$, where the latter value is based on a typical soil Poisson ratio [36]. This gives us a total of 8 different cases. The cell problems are solved on a single unit cell using Comsol multiphysics, v5.2. Comsol is a commercial finite element package which allows the equations to be coded using the in built "general form PDE" package. The results of the cell problems are shown in figure 5.

From these results the effective parameters can be calculated and the homogenised equations can be compared to the full equations. The result of the comparison is shown for different values of r_a, r_s and ν in figures 6 and 7. We see that the homogenised equations provide a good approximation of the force response to the applied displacement. The error is largest, $\lesssim 2\%$ for the particle of radius $r_a = 0.3$ and $r_s = 0.3$, and decreases for smaller particles, $\lesssim 0.2\%$ for particles of radius $r_a = 0.1$ and $r_s = 0.1$.

4. Discussion and Conclusion

The method described here allows the macroscopic properties of a poro-elastic composite to be determined based on knowledge of the underlying structure. The method is based on the technique of homogenisation and relies on solving a series of representative cell problems on a known geometry. The result is a coupled set of three partial differential equations, which are analogous to the standard Biot equations for poro-elastic materials. Biot's equations are well known in the literature and have been widely applied in the field of geomechanics [4], accoustic propagation in snow [37], and biomechanics [38]. The equations that we have derived differ from

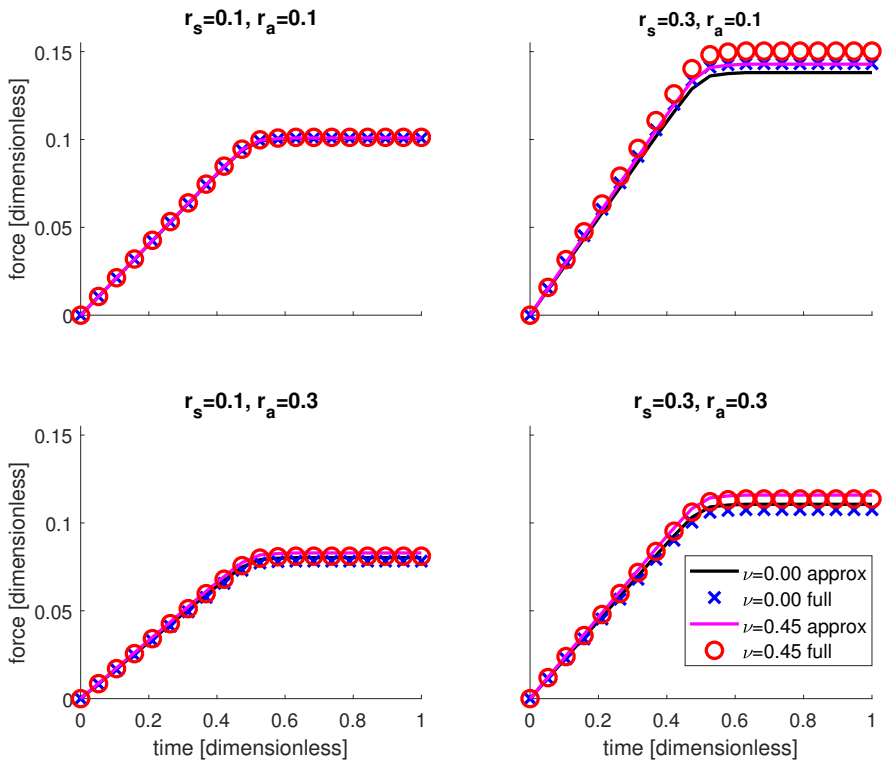

Figure 7. Validation of homogenised equations in simple shear test. The plots show the force measured due to a ramped displacement of the form given in equation (3.2).

the standard Biot poro-elastic theory in that they describe an elastic structure interacting with two fluids, air and water. In addition, we have considered the large deformation limit resulting in an additional set of non-linear terms in the averaged theory.

In order to provide a minimum validation for this model we have compared the approximate equations to the original governing equations and shown that the differences between these two cases are less than 2% for the geometries tested. Whilst it is not clear that this will be the case for all geometries it is suggestive that the method works for isotropic soil samples. The method developed here is not restricted to the idealised geometry used for validation. The geometries were chosen such that the full equations could be solved without significant computational difficulty. In fact, the method here can be readily applied to any soil geometry either created in-silico or imaged using, for example, X-ray Computed Tomography.

There are several additional problems, which must be considered before applying these methods to images obtained from X-ray Computed Tomography. Firstly, once imaged the soils will need to be segmented and computational meshes generated. These steps are non-trivial, see the review by Roose *et al* [39], and will be further complicated as each solid grain will need to have individual physics assigned to it. Secondly, we have assumed that our underlying geometry is periodic, *i.e.*, it is made up of regularly repeating units. Even well sieved soils are not periodic and assumptions have to be made regarding the soils structure. Typically, this is tackled by considering a sufficiently large volume of soil, often referred to as a Representative Volume Element (RVE). Once the RVE is sufficiently large the lack of periodicity on the boundaries becomes insignificant in comparison to the bulk soil behaviour and the representative properties can be calculated [29]. In doing so assumptions have to be made regarding the boundaries of

the domain. These can either be assumed to have known constitutive behaviour or periodicity can be enforced through reflection [40]. Finally, the amount of data generated in solving such problems can be significant and such image based simulations are typically carried out on large supercomputers. Notwithstanding the challenges, such a study would be worthwhile as it would enable macroscopic poro-elastic properties to be optimised based on design and manipulation of microscopic poro-elastic properties.

The method relies on a number of assumptions regarding the underlying structure. Firstly, we have considered only three phases; solid grains, incompressible gas and a Biot poro-elastic mixed phase containing water and elastic solids, three phases commonly seen in X-ray Computed Tomography images of real soils. These phases do not exhaustively describe the phases present in soil. Other phases may be present, for example, water which is not held in the mixture phase. Fundamentally there is no reason why such a phase could not be added to this model and described, for example, using a Cahn-Hilliard-Stokes model such as the one used in [21] and combining the ideas of [26]. Whilst, such an addition would be worth while it would add significant complications to the derivation and resulting models.

Of the phases considered several assumptions are made. Firstly the air phase is assumed deformable, but incompressible. Secondly the rigid particles move through rigid body translations. Finally, no solid-solid interactions occur. These assumptions are not fundamental to the development of the theory, however, they significantly simplify the physics involved making the equations and the numerical solutions tractable. In principle these assumptions could easily be relaxed by adding additional physics at the start and proceeding with the same approach.

Despite the assumptions this method has been developed to allow the macroscopic poro-elastic properties of materials to be derived based on knowledge of the local structure. Such a method will be widely used in the prediction and analysis of complex composite pore structures such as soils and will enable the direct prediction of their properties from representative X-ray Computed Tomography images.

Data accessibility

This paper has no data

Competing interests

The authors have no conflict of interest to declare

Authors' contributions

KRD derived the equations and undertook the homogenisation, numerical modelling and paper writing. TR designed the study and was consulted on the derivation and paper writing.

Acknowledgements

The authors also acknowledge members of the "Rooty Team" at University of Southampton for helpful discussions related to this work.

Funding

KRD and TR are funded by ERC646809DIMR.

Ethics statement

This work did not include any work on humans.

References

1. Maurice A Biot.
General theory of three-dimensional consolidation.
Journal of applied physics, 12(2):155–164, 1941.
2. Maurice A Biot.
Theory of elasticity and consolidation for a porous anisotropic solid.
Journal of applied physics, 26(2):182–185, 1955.
3. MA Biot and DG Willis.
The elastic coeff cients of the theory of consolidation.
J. appl. Mech, 24:594–601, 1957.
4. Herbert Wang.
Theory of linear poroelasticity with applications to geomechanics and hydrogeology.
Princeton University Press, 2000.
5. James R Rice and Michael P Cleary.
Some basic stress diffusion solutions for fluid-saturated elastic porous media with compressible constituents.
Reviews of Geophysics, 14(2):227–241, 1976.
6. Dani Or and Teamrat A Ghezzehei.
Modeling post-tillage soil structural dynamics: a review.
Soil and Tillage Research, 64(1):41–59, 2002.
7. Stephan Peth and Rainer Horn.
The mechanical behavior of structured and homogenized soil under repeated loading.
Journal of Plant Nutrition and Soil Science, 169(3):401–410, 2006.
8. S Peth, J Nellesen, G Fischer, and R Horn.
Non-invasive 3d analysis of local soil deformation under mechanical and hydraulic stresses by μct and digital image correlation.
Soil and Tillage Research, 111(1):3–18, 2010.
9. Muhammad Farrakh Nawaz, Guilhem Bourrie, and Fabienne Trolard.
Soil compaction impact and modelling. a review.
Agronomy for Sustainable Development, 33(2):291–309, 2013.
10. Robert Burridge and Joseph B Keller.
Poroelasticity equations derived from microstructure.
The Journal of the Acoustical Society of America, 70(4):1140–1146, 1981.
11. Cheo K Lee and Chiang C Mei.
Re-examination of the equations of poroelasticity.
International journal of engineering science, 35(4):329–352, 1997.
12. Robert E Gibson, Robert L Schiffman, and Kenneth W Cargill.
The theory of one-dimensional consolidation of saturated clays. ii. finite nonlinear consolidation of thick homogeneous layers.
Canadian geotechnical journal, 18(2):280–293, 1981.
13. M Th Van Genuchten.
A closed-form equation for predicting the hydraulic conductivity of unsaturated soils.
Soil Science Society of America Journal, 44(5):892–898, 1980.
14. A. Carminati and D. Vetterlein.
Plasticity of rhizosphere hydraulic properties as a key for efficient utilization of scarce resources.
Annals of Botany, 2012.
15. Murray Fredlund, Jim Zhang, Dirk van Zyl, and Sean Wells.
Multidimensional coupled sedimentation and consolidation theory.
In *Tailings & Mine Waste*, pages 15–17, 2012.
16. U. Hornung.
Homogenization and Porous Media.
Springer, 1996.
17. G. A. Pavliotis and A. M. Stuart.
Multiscale Methods Averaging and Homogenization.
Springer, New York, 2000.
18. Grégoire Allaire.

Homogenization and two-scale convergence.
SIAM Journal on Mathematical Analysis, 23(6):1482–1518, 1992.

19. L. Tartar.
Incompressible fluid flow in a porous medium-convergence of the homogenization process.
Appendix of [16]. T. Muthukumar Department of Mathematics, Indian Institute of Science, Bangalore-560012, India E-mail address: tmk@ math. iisc. ernet. in, 1980.
20. J.B. Keller.
Darcy's law for flow in porous media and the two-space method.
Nonlinear Partial Differential Equations in Engineering and Applied Science, 54, 1980.
21. Keith R Daly and Tiina Roose.
Homogenization of two fluid flow in porous media.
Proceedings of The Royal Society A: Mathematical Physical and Engineering Sciences, 471(2176):2014056–1, 2015.
22. K. Zygalakis and T. Roose.
A mathematical model for investigating the effect of cluster roots on plant nutrient uptake.
The European Physical Journal - Special Topics, 204:103–118, 2012.
10.1140/epjst/e2012-01555-9.
23. K.C. Zygalakis, G.J.D. Kirk, D.L. Jones, M. Wissuwa, and T. Roose.
A dual porosity model of nutrient uptake by root hairs.
New Phytologist, 192:676ï£¡688, 2011.
24. Maria Bruna and S Jonathan Chapman.
Diffusion in spatially varying porous media.
SIAM Journal on Applied Mathematics, 75(4):1648–1674, 2015.
25. Eduard Rohan, Simon Shaw, and John R Whiteman.
Poro-viscoelasticity modelling based on upscaling quasistatic fluid-saturated solids.
Computational Geosciences, 18(5):883–895, 2014.
26. K.R. Daly and T Roose.
Multiscale modelling of hydraulic conductivity in vuggy porous media.
Proc. R. Soc. A, 470:20130383, 2013.
27. Eduard Rohan, Salah Naili, and Thibault Lemaire.
Double porosity in fluid-saturated elastic media: deriving effective parameters by hierarchical homogenization of static problem.
Continuum Mechanics and Thermodynamics, 28(5):1263–1293, 2016.
28. NB Nguyen, A Giraud, and D Grgic.
A composite sphere assemblage model for porous oolitic rocks.
International Journal of Rock Mechanics and Mining Sciences, 48(6):909–921, 2011.
29. A Giraud, NB Nguyen, and D Grgic.
Effective poroelastic coefficients of isotropic oolitic rocks with micro and meso porosities.
International Journal of Engineering Science, 58:57–77, 2012.
30. AC Fowler and CG Noon.
Mathematical models of compaction, consolidation and regional groundwater flow.
Geophysical Journal International, 136(1):251–260, 1999.
31. PJ Vardanega and MD Bolton.
Stiffness of clays and silts: Normalizing shear modulus and shear strain.
Journal of Geotechnical and Geoenvironmental Engineering, 139(9):1575–1589, 2013.
32. Mary Beth Kirkham.
Principles of soil and plant water relations.
2014.
33. Jacob Bear.
Dynamics of fluids in porous media.
1972.
34. Keith R Daly, Samuel D Keyes, Shakil Masum, and Tiina Roose.
Image-based modelling of nutrient movement in and around the rhizosphere.
Journal of experimental botany, 67(4):1059–1070, 2016.
35. LW Zachary and RA Lohnes.
Confined compression test for soils.
Transportation Research Record, (1278), 1990.
36. UE Essien, AO Akankpo, and MU Igboekwe.

Poisson's ratio of surface soils and shallow sediments determined from seismic compressional and shear wave velocities.
International Journal of Geosciences, 5(12):1540, 2014.

37. Achille Capelli, Jagdish C Kapil, Ingrid Reiweger, Dani Or, and Jürg Schweizer.
Speed and attenuation of acoustic waves in snow: Laboratory experiments and modeling with biot's theory.
Cold Regions Science and Technology, 125:1–11, 2016.
38. Antony PS Selvadurai.
Mechanics of poroelastic media, volume 35.
Springer Science & Business Media, 2013.
39. T Roose, SD Keyes, KR Daly, A Carminati, Wilfred Otten, D Vetterlein, and S Peth.
Challenges in imaging and predictive modeling of rhizosphere processes.
Plant and Soil, 407(1-2):9–38, 2016.
40. S.R. Tracy, K. R. Daly, C.J. Sturrock, N.M.J Crout, S.J. Mooney, and T. Roose.
Three dimensional quantification of soil hydraulic properties using x-ray computed tomography and image based modelling.
Submitted to WRR, 2014.